Coastal submesoscale processes and their effect on phytoplankton distribution in the SE Bay of Biscay

Xabier Davila[1], Anna Rubio[1], Luis Felipe Artigas[2], Ingrid Puillat[3], Ivan Manso-Narvarte[1], Pascal Lazure[3], and Ainhoa Caballero[1]

[1]AZTI Marine Research, Basque Research and Technology Alliance (BRTA), Herrera Kaia, Portualdea z/g, 20110 Pasaia, Spain

[2]Université du LIttoral Côte d'Opale, Université de Lille, CNRS UMR 8187 LOG, Wimereux, France.

[3]IFREMER/Dyneco/Physed, BP 70, 29280 Plouzané, France.

Correspondence: Xabier Davila (Xabier.Davila@uib.no)

Abstract.

Submesoscale processes have a determinant role in the dynamics of oceans by transporting momentum, heat, mass and particles. Furthermore, they can define niches where different phytoplankton species flourish and accumulate, not only by nutrient provisioning, but also by modifying the water column structure or by active gathering through advection. In coastal areas, however, submesoscale oceanic processes act together with coastal ones, and their effect on phytoplankton distribution is not straightforward. The present study brings into consideration the relevance of hydrodynamic variables, such as vorticity, in the study of phytoplankton distribution, from the analysis of in-situ and remote multidisciplinary data. In-situ data were obtained during the Etoile oceanographic cruise, which surveyed the CapBreton canyon area in the South-East of Bay of Biscay in early August 2017. The main objective of this cruise was to describe the link between the occurrence and distribution of phytoplankton spectral groups and mesoscale to submesoscale ocean processes. In-situ discrete hydrographic measurements and multi-spectral chlorophyll-a (chl-a) fluorescence profiles were obtained in selected stations, while temperature, conductivity and in-vivo chl-a fluorescence were also continuously recorded at the surface. On top of these data, remote sensing data available for this area, such as High Frequency radar and satellite data, were also processed and analysed. From the joint analysis of these observations, we discuss the relative importance and effects of several environmental factors on phytoplankton spectral groups distribution above and below the pycnocline, and at the Deep Chlorophyll Maximum (DCM) by performing a set of Generalized Additive Models (GAMs). Overall, salinity is the most important parameter modulating not only total chl-a but also the contribution of the two dominant spectral groups of phytoplankton, Brown and Green algae groups. However, at the DCM, among the measured variables, vorticity is the main modulating environmental factor for phytoplankton distribution and explains 19.30 % of the variance. Since the observed distribution of chl-a within the DCM cannot be statistically explained without the vorticity, this research sheds light on the impact of the dynamic variables in the distribution of spectral groups at high spatial resolution.

1 Introduction

The monitoring and characterization of submesoscale dynamics are determinant for the appropriate comprehension of marine ecosystems (Lévy et al., 2012). Submesoscale processes refer to those features that range on spatio-temporal scales on the order of 0.1 - 10 km and days. The timescales at which these processes evolve make them uniquely important to the structure and functioning of planktonic ecosystems (Lévy et al., 2012; Mahadevan, 2016). They influence the ecosystem by either driving episodic nutrient pulses to the sunlit surface, by affecting the mean time that photosynthetic organisms remain in the well-lit surface (Lévy et al., 2012), or by reducing and even suppressing the biological production (Gruber et al., 2011). In addition, since primary production drives the absorption of atmospheric CO_2, submesoscale processes might actively contribute to the carbon export and regulate the fate of particulate organic carbon (Mahadevan, 2014). The effect of submesoscale processes on phytoplankton has also implications for regional biogeochemical budgets, plankton monitoring strategies, fisheries, and management (Irigoien et al., 2007).

The influence of ocean dynamics on phytoplankton covers a wide range of spatio-temporal scales, and these are inherent to the surveying strategy to be selected. D'Ovidio et al. (2010) linked the occurrence of different phytoplankton groups with the large-scale surface ocean dynamics, based on altimetry data. They defined the so-called fluid dynamical niches where the phytoplankton assemblages occur within distinct physicochemical environments. However, available satellite observations lack the spatio-temporal resolution to properly resolve the fast-evolving submesoscale coastal processes. In coastal regions, where oceanic currents meet the sea floor, the connection between the submesoscale processes and phytoplankton becomes even more challenging, and therefore requires more demanding surveying methods that can provide a high spatio-temporal resolution. Nowadays, autonomous gliders can typically cover 1 km horizontally in an hour, but even this can be too slow for synoptic measuremets of larger submesoscale features (on scales of 10 km). An alternative is the use of ship-towed undulating devices, which allow sampling 10-20 times faster than a glider (Lévy et al., 2012). Regarding phytoplankton distribution, sub-mesoscale to microscale vertical patterns of chlorophyll-a (chl-a) concentration have been studied widely by the use of in vivo fluorometric casts, allowing to identify the Deep Chlorophyll Maximum (DCM) (Cullen, 2015). Differences within the DCM in terms of concentration, biomass and diversity stress the importance of the environmental drivers involved (Latasa et al., 2017), on which the occurrence of (sub)mesoscale processes play a critical role (Lévy et al., 2012).

This study focuses on the innermost South-Eastern region of the Bay of Biscay (SE-BoB), a semi-open bay limited by the Spanish coast in the southern part and the French coast in the eastern part. The BoB is an area of complex coastal hydrographic and hydrodynamic processes, mainly due to the intricate bathymetry, the seasonally modulated and episodically strong river runoff, the wind- and density-driven ocean circulation and their interplay. The circulation in the coastal SE BoB is controlled mainly by the prevailing winds, although the general pattern is characterised by a weak anticyclonic circulation in the central deeper region (Valencia et al., 2004; Pingree and Garcia-Soto, 2014). The wind pattern either reinforces or weakens the seasonal Iberian Poleward Current (IPC), which flows cyclonically over the slope in autum and winter (Rubio et al., 2013).

The IPC is, due to the effect of bathymetry, responsible for the generation of Slope Water Oceanic eDDIES (SWODDIES) (Caballero et al., 2016; Teles-Machado et al., 2016). Besides, the ocean surface layer in this region is subjected to the seasonal variations of the water runoff from the main nearby rivers: Gironde, Loire and Adour (Reverdin et al., 2013). The river runoff significantly modifies the water mass adjacent to the shelf by creating turbid and dilution plumes (Ferrer et al., 2009), which act as a nutrient source to the surface layers and sustain primary production in the region (Morozov et al., 2013).

These complex ocean dynamics can modulate phytoplankton occurrence in the BoB. The flow of the IPC generates a shelf-break convergent front that separates the advected high-salinity and warm waters from the cold fresher coastal waters. The vertical mixing associated with this frontal system has a substantial influence on the whole plankton community (Fernández et al., 1993). Caballero et al. (2016) reported a DCM in the centre of a SWODDY resulting from the vertical velocities and eddy-wind induced Ekman pumping in the centre of the anticyclone. More recently, Muñiz et al. (2019) described the phytoplankton annual cycle on the SE-BoB and reported that temperature and nutrients explained most of the of the variability of chl-a concentration. Nevertheless, to our knowledge, none of these studies have focused on the relative importance of submesoscale dynamics, analyzing hydrographic and hydrodynamic forcing mechanisms at the same time.

In order to shed light on the coastal submesoscale dynamics and their effects on chl-a and phytoplankton groups distribution, the Etoile oceanographic cruise surveyed the CapBretron Canyon area early August 2017. This cruise was one of the research actions in the framework of the European H2020 Joint European Research Infrastructure for Coastal Observatory - Novel European eXpertise for coastal observaTories (JERICO-NEXT) project. The regional coastal observatories (EuskOOS) are also embedded in the JERICO Research Infrastructure and provide the operational HF radar data complementing the Etoile in-situ measurements. Both JERICO-NEXT (2014 - 2019), its predecessor JERICO (2007 - 2013) and the ongoing JERICO-S3 (2020 - 2024), aim to consolidate of a pan-European coastal observatory infrastructure, for a better understanding of the functioning of coastal marine systems and a better assessment of their changes. In this study, we first describe the submesoscale processes that are present in the study area based on the joint analysis of a wide range of multiplatform spatio-temporal data, from remote sensing to in-situ measurements. Secondly, we investigate the link between the observed submesoscale structures and the distribution of the two dominant spectral groups of phytoplankton, estimated with multi-spectral chl-a fluorescence technique, above and below the pycnocline, and at the DCM, by performing a set of General Additive Models.

2 Material and Methods

2.1 In-situ data from the Etoile cruise

In the framework of the European H2020 JERICO-NEXT project, the "Côtes de la Manche" research vessel (CNRS-INSU), surveyed the area of CapBreton canyon from August 2nd to 4th 2017 during the Leg 2.2 of the Etoile oceanographic cruise (P.I. Pascal Lazure, IFREMER, DOI: 10.17600/17010800), aiming to unravel the mesoscale and submesoscale dynamics in the area. The cruise consisted in six transects covering the continental shelf and slope, as well as the axis of the canyon, as shown

in Figure 1. During east-west transects (T1, T3 and T5) a CTD (Sea-Bird) was deployed every ∼7 km, while during west-east transects (T2, T4 and T6) a Moving Vessel Profiler (MVP200 operated by Genavir) was towed and the profiles were averaged every 5 km. As a good compromise in terms of spatial resolution and coverage of the observations was important, the use of the Moving Vessel Profiler (MVP) allowed a more extensive and quicker sampling suitable for small, rapidly evolving structures.

During the cruise, chl-a was estimated by a FluoroProbe (Bbe Moldakenke) multi-spectral fluorometer, which measured chl-a and accessory pigments using light-emitting diodes (LEDs) with different wavebands. Therefore, it was possible to distinguish between four algal pigmentary groups: "Blue algae" (e.g. phycocyanin-containing Cyanobacteria), "Green algae" (e.g. Chrolorophytes, Chrysophytes), "Brown algae" (e.g. Diatoms, Dinoflagellates) and "mixed red group" (e.g. phycoerythrin-containing Cyanobacteria, Cryptophytes). The FluoroProbe estimated chl-a equivalent (ChlaEQL) concentrations for these four groups and Total chl-a following the algorithms of Beutler et al. (2002) as explained in MacIntyre et al. (2010) and a manufacturer's calibration, and also provided an estimation of the concentration of chromophoric dissolved organic matter (CDOM or yellow substances). Up to 80 m depth in-vivo chl-a profiles were obtained. Unfortunately, this data could just be gathered in the T3 and T5 transects due to connection issues with the instrument during T1. During the whole cruise salinity and in-vivo chl-a were continuously measured on surface (3.5 m deep) by a thermosalinograph and a second automated FluoroProbe multi-spectral fluorometer, respectively.

2.2 Complementary operational remote sensing data

In addition to the in-situ data, remote sensing operational data was used to complete the picture obtained during Etoile. Ocean surface currents measurements were obtained by two long-range high-frequency (HF) radar antenna located at Matxitxako and Higer Capes. The antennas are owned by the Directorate of Emergency Attention and Meteorology of the Basque Security Department, and are part of EuskOOS network (euskoos.eus/en). They emit at a central frequency of 4.463 MHz and a 30-kHz bandwidth, and provide hourly horizontal currents maps (corresponding to vertically integrated horizontal velocities in the first 3 m of the water column) (Rubio et al., 2013). The receiving signal, an averaged Doppler backscatter spectrum, allows to estimate surface currents over wide areas (reaching distances over 100 km from the coast) with high spatial (1-5 km) and temporal (≤1 h) resolution (Figure 1B). To obtain the surface velocity data we followed the methodology detailed in Rubio et al. (2013). Velocity data is processed from the spectra of the received echoes every 20 minutes using the MUSIC (MUltiple SIgnal Classification) algorithm. Then, a centred 3h running average was applied to the resulting radial velocity fields as part of the pre-processing previous to the computation of total currents. The current velocity data were quality controlled using procedures based on velocity and variance thresholds, signal-to-noise ratios, and radial total coverage, following standard recommendations (Mantovani et al., 2020). The performance of this system and its potential for the study of ocean processes and transport patterns have already been demonstrated by previous works (e.g. Rubio et al. (2011, 2018); Solabarrieta et al. (2014); Caballero et al. (2020)).

In order to visualize representative velocity fields, we applied a 10th order digital Butterworth low-pass filter (Emery and Thomson, 2001) to both velocity components at each node (filtering out T<48 h). Therefore, HF processes such as inertial currents or tides were removed, as these are irrelevant for this study and would have eclipsed the geostrophic and wind-induced current mesoscale and submesoscale patterns. A Lagrangian Particle-Tracking Model (LPTM) was applied to HF radar data to simulate trajectories and analyse surface ocean transport patterns around the dates of the Etoile survey. Particles released within the HF radar coverage area were advected using a 4th order Runge–Kutta scheme (Benson, 1992). In this case, the particles are advected using the 2D hourly current fields given by the HF radar from July 26th to August 11th. To describe (sub)mesoscale patterns, Lagrangian Residual Currents (LRC) were calculated following a methodology similar to that described in Muller et al. (2009), using an integration time of 3 days.

Furthermore, satellite data prior to and after the cruise was also analysed. Sea Surface Temperature (SST) and satellite chl-a data (chl-a^{sat}) were retrieved from the Visible and Infrared Imager/Radiometer Suite (VIIRS) sensor and water turbidity from MODIS. In addition to these datasets, hourly wind information of July and August was collected by the mooring buoy of Bilbao owned by Puertos del Estado (available in www.puertos.es). Although its location is not exactly in our study area (Figure 1B) it is considered close enough for a general description of the wind regime in the bay.

2.3 Computation of vorticity and vertical velocities

From hydrographic data alone, geostrophic circulation can be diagnosed, inferring various key dynamical variables such as geostrophic relative vorticity (hereinafter referred to just as vorticity) or the vertical velocity from a 3D snapshot of the density field. To compute vertical velocities, we assume quasi-geostrophic dynamics and a synoptic or steady state, where the Rossby number is small (Ro = U/f L «1, where U is the characteristic velocity, L is length scale and f the Coriolis parameter) and submesoscale features remain constant during the sampling (Gomis et al., 2001). To reduce the computational effort during the analysis of the data, the MVP transects were averaged every 5 km, considering it enough resolution for resolving submesoscale structures, following the methodology in Gomis et al. (2001). An interpolation of the data allows deriving key dynamical variables, such as the geostrophic relative vorticity and vertical velocities. This was accomplished by merging the CTD and averaged MVP profiles after verifying that no significant bias was present between the measurements of these two instruments. Once having verified that data can be merged, the Optimal Statistical Interpolation (OSI) was performed by the 'DAToBJETIVO' software package developed by Gomis and Ruiz (2003), for the objective spatial analysis and the diagnosis of oceanographic variables.

For the interpolation in the sampling area, an 11 x 33 output grid was used with a 0.031° x 0.033° resolution (Figure 1A), pursuing a compromise between providing a good representation of the scales that can be resolved by the sampling and minimizing the effect of the observational error. A Gaussian function for the correlation model between observations (assuming 2D isotropy) was set up, with a correlation length scale of 15 km. The noise-to-signal (NTS) variance ratio used for the analysis

of temperature, salinity and dynamic height were: 0.01, 0.005, and 0.0027, respectively. This ratio was defined as the variance of the observational error divided by the variance of the interpolated field (the latter referring to the deviations between observations and the mean field). This parameter allows the inclusion in the analysis of an estimation of the observational error and adjustments of the weight of the observations on the analysis (the larger the NTS parameter, the smaller the influence of the observation). Then, after the interpolation, all fields were spatially smoothed, with an additional low-pass filter with a cut-off length scale of 10 km to avoid aliasing errors due to unresolved structures. This resulted in a coarse grid that allowed the appropriate representation of the subsequent spatial derivatives of the analysed field. In the vertical, 98 equally-spaced levels were considered, from 4 to 200 m (every 2 m). To analyse and correlate the explanatory and the response variables, the same interpolation was performed for the chl-a data.

2.4 Statistical Analysis

The presence of a well-defined seasonal pycnocline and a DCM were used as criteria to define three dynamically different layers in the water column, which have been analysed separately to constrain the different dynamical environments. Therefore, prior to the statistical analysis, the dataset was divided in three subsets: "Above the pycnocline" ("APY", containing data from 4 to 24 m depth), "Below the pycnocline" ("BPY", containing data from 26 to 74 m depth) and "at the DCM" ("DCM", containing data from 26 to 74 m and where Total chl-a ≥ 1.5 μg ChlaEQL^{-1}).

We assessed the relative importance of different environmental factors involved in the phytoplankton distribution by developing a Generalized Additive Model (GAM) statistical model (Hastie and Tibshirani, 1990). GAMs offer the possibility of identifying non-linear relationship between variables by the inclusion of a smoothing function that has no specific shape. Since the relationship among variables along the entire water column might mask each other, three GAMs were implemented for the different dynamical environments in the water column, previously detailed, by using (Equation 1):

$$[Chl-a]_z = a + g_1[Sal_z] + g_2[Temp_z] + g_3[Vor_z] + g_4[V.Vel_z] + \epsilon \tag{1}$$

Where a is an intercept, z is the location in the water column ('APY', 'BPY' and 'DCM'), the gs are nonparametric smooth functions describing the effect of environment on chl-a concentrations and ϵ is an error term. Sal, Temp, Vor and V.Vel correspond to the environmental variables determined in this study, salinity, temperature, vorticity (cyclonic/anticyclonic) and vertical velocities (upwelling/downwelling), respectively.

In order to account for co-linearity problems, we calculated pairwise Spearman correlation coefficients (r) between variables. The only pair of variables correlated were salinity and temperature for the BPY subset (r = -0.77, *p-value*<0.05) related to the depth dependency of both variables. The model selection was based on the analysis performed by Llope et al. (2009) where a stepwise approach was implemented by removing covariates and minimizing the generalized cross-validation (GCV) criterion

of the model (Wood, 2000). The GCV criterion is a measure of the out-of-sample predictive performance of the model and is related to the Akaike's Information Criterion (AIC) (Wood, 2006). Similarly, by deleting one variable at a time we can quantify the penalty on the explained variance of the phytoplankton distribution (Llope et al., 2009). In total, 12 GAMs were carried out from the combination of Total chl-a, Green algae chl-a (Green chl-a), Brown algae chl-a (Brown chl-a) and Brown chl-a to Green chl-a ratio (B:G) among the three vertical subsets (Table 1). All the variables showed a significant impact on the Total and group chl-a distribution except the vorticity for the Green chl-a in the APY subset. If vorticity was removed, the model slightly improved (GCV decreased from 0.0130 to 0.0125; Table 2). Yet, we decided to keep it in the model for the different levels, having in mind that its impact in the APY subset was insignificant. In addition, vertical velocities for the APY subset show unrealistic values as an artefact of the surface boundary condition necessary to perform the calculations, where velocities are assumed to be null. Since the derived relationships with chl-a are not considered realistic, even if included in the analysis and slightly improving the models, they are not further considered. The rest of the variables, even if they explained a small part of the variance, they significantly improved the model. The GAMs were carried out by using R (version 3.63, R Core Team (2020)) and the package mgcv (version 1.8.33) (Wood, 2011).

3 Results

3.1 Mapping coastal mesoscale hydrography and currents

The combined use of wind data and satellite imagery together with the HF radar provide a context of hydrographical and dynamical regime around the dates of the Etoile cruise. Figure 2 shows the Progressive Vector Diagram (PVD) of the wind conditions. From July 21st to 28th, the predominant wind has a marked north-westerly component with relatively high intensity. Afterwards, it decreases in intensity, shifts and starts blowing from the north-east. On August 7th the wind has again a north-west component for few days. Therefore, the wind conditions during the whole cruise remain almost constant in direction and low in intensity. Figure 3 shows the satellite SST, chl-a^{sat} and turbidity fields; the latter allowed us to locate the river plumes of the Adour and the Bidasoa rivers. In addition, the LRC fields derived from the HF radar, which and superimposed to the previous fields, give a high-resolution image of the surface transport during the days previous to the survey, in the periods July 26-29th and July 30th to August 2nd. The surface circulation patterns and position of the river plumes are observed to evolve from the first to the second periods. In July 26-29th (Figure 3 – left column), under north-westerly winds the circulation shows complex spatial patterns, and two cyclonic eddies, with diameters between 10-15 km, can be identified (C17W at 43.6°N and 2°W and C17E at 43.7°N and 1.7°W). During the period July 30th to August 2nd (Figure 3 – right column), the winds shift to north-easterly, which generates a remarkable transition to westward currents. At this moment, the cyclonic eddies are not visible by the HF radar. Instead, in their position, we observe a meandering pattern that affects the distribution of the SST, the position of the river plumes and their associated chl-a^{sat} signature. In addition, on August 2nd, a sharp decrease in SST is observable close to the French inner shelf, which is linked with the upwelling generated by the north-easterly winds.

During the Etoile cruise (August 2nd to 4th), the first meters of the water column are characterized by a high spatial variability (Figure 4). Although the river plume is not visible anymore in the salinity fields at 14 m, a layer of relatively fresh water is located in the inner continental shelf (1.6 – 1.7°W). This low salinity front extends over 20 km horizontally and 18 m vertically (Figure 5A), if we consider the isopycnal 35.1 as in Puillat et al. (2006). At 60 m depth (Figure 4), a second salinity front is observed at the shelf break (i.e. along the 250 m isobath), with a vertical extension between 50 and 120 m (Figure 5). Fresher waters, with salinities of ∼35.5 occupy the totality of the water column over the shelf, while oceanic waters at the slope are characterized by salinities over ∼35.6. The salinity range in the shelf break front is much smaller than in the surface front.

The cyclones depicted in Figure 3 are also observed at deeper layers in the vorticity and geostrophic velocities fields, while they do not have a clear surface signature during the days of the cruise. The disappearance of the C17W and C17E in the LRC fields during the cruise period coincides with a change in the wind pattern, which results in a surface wind-driven flow that masks the geostrophic circulation at surface. Few days after, once the wind changes back to a north-west component, C17W is observable again in the HF radar (See Supplementary Material Figure A1), suggesting a persistent nature. Noteworthy, the vorticity fields also show an anticyclone (A17) at the NW part of the domain (centred at 43.80°N 2.25°W), although this is not observed in the HF radar fields. In addition to A17, a region of anticyclonic vorticity is well defined in the frontal area between the cyclones. At 60 m the cyclonic eddies present a negative temperature anomaly and relative higher salinity values. A17 is associated to a positive temperature anomaly and higher salinity. Associated to the frontal areas in the two dipoles (A17-C17W and C17W-C17E) we observe two main upwelling areas (positive vertical velocities), whose maxima have a relatively constant position throughout the water column.

From the cross-section at 43.77°N, we can observe the vertical extension of both the low salinity surface front and the shelf break salinity front (Figure 5A). The surface salinity front has a vertical extension of ∼20 m, while the location of the shelf break front is at ∼50-110 m. The uplift and depression of the isopycnal lines (black contours) is coherent with the presence of submesoscale structures of different polarity, mostly following the temperature distribution. These two variables contribute to the water density and the position of the seasonal pycnocline at ∼25 m, primarily conditioned by the warming of surface waters in summer. From the vorticity field and the geostrophic meridional velocities (Figure 5D), it is noticed that the position of the anticyclonic frontal area between C17W and C17E coincides with the shelf break (1.9°W) and its strength decreases with depth from a maximum at 25 m. The onshore area is dominated by a southward flow while the offshore area is dominated by a northward flow. As in Figure 4, the highest vertical velocities are located in the eddies' periphery, where the largest vorticity gradients are located.

3.2   Chlorophyll-a and spectral groups distribution

Surface chl-a (from the continuous recording surface Fluoroprobe) shows a distribution spatially dependent on salinity at 3.5 m depth, related to the position of the river plume (Figure 6). The chl-a maximum is observed around the salinity minimum,

255 decreasing to the NW (and with depth) in accordance with the increase of salinity. Vertically, the 43.77°N cross-section shows a complex distribution of Total chl-a and spectral groups (Figure 7). Two DCMs are observed, one over the inner shelf at ~30-50 m, and the second over the shelf edge, at ~50-65 m, below the pycnocline. The shallow DCM is split into two cores, although its morphology is hard to assess due to the limited spatial coverage of the sampling. The deep DCM, is located at the anticyclonic frontal area between C17W and C17E and is compose mainly by the Brown algae, the dominant spectral group.

260 The maximum is centred in the anticyclonic frontal area between C17W and C17E. Green algae, however, follow a different pattern and are distributed slightly deeper, following the salinity contours over 35.55. The ratio between Brown chl-a and Green chl-a (B:G), logarithmically transformed, provides an even clearer image of how the different spectral groups are distributed. There is a sharp transition between the Brown algae (around the anticycloninc frontal area) and the Green algae (below the 35.55 isohaline). The 43.70°N cross-section (See Supplementary Material Figure A2), which is not crossing the core of the

265 anticyclonic front, reveals that this pattern is not ubiquitous. Here, there is not a clear dichotomy among the groups nor a deeper maximum of Green algae.

3.3 Exploring bio-physical impacts

The results of the GAMs in the APY subset (Figure 8, Table 1) suggest that overall, all the models perform well, explaining in

270 all cases more than 40 % of the variance. Salinity and temperature contribute to most of the variance of the model and explain the 13.10 % and 9.8 % of it, respectively (Table 2). As expected in agreement with Figure 6, lower salinity values are associated with higher Total chl-a concentration, showing a negative relationship (Figure 8a). Regarding the effect of temperature, it follows a convex-shape function, with a minimum at ~ 22°C (Figure 8b), while the contribution of vorticity (Figure 8c) is very small. The response of Brown chl-a differs from the Total chl-a, although salinity still explains most of the variance of

275 the model (23.3 %). Brown chl-a shows a dome-shape response to salinity (Figure 8e) with a maximum at ~35.1 (i.e. waters fresher or saltier than 35.1 have a negative impact) and a positive response to positive (cyclonic) vorticity. Green chl-a almost mimics the distribution of Total chl-a (Figure 8i-m), excepting the non-significant relation with vorticity (*p-value*>0.05). For Green algae temperature and salinity explain 10.40 % and 12.70 % of the variance, respectively. Note that, in this case, the removal of salinity has no penalty in the explained variance, likely owing to the temperature capturing most of the variability.

280 The B:G ratio shows dome-shape relationships for salinity and temperature, where the maxima are at ~35.2 and ~ 22°C (Figure 8n and 8l). At fresher and or warmer waters higher concentrations of Green algae are observed. The contributions of both salinity and temperature to the variance are similar, 15.6 % and 15.8 %, respectively.

In the BPY subset, the GAMs explain a larger percentage of the variance and generally perform better than for the APY

285 subset (except for the Green algae), and suggest a different response of the chl-a to the environmental variables (Table 1, Figure 9). We observe a negative correlation between chl-a and salinity until values of ~35.5 (Figure 9a) and a dome-shape behaviour with temperature (34 % of explained variance), with a maximum at ~14 °C (Figure 9b, Table 2). Although the explained variance by vorticity is small, there is a clear positive trend in chl-a with negative or anticyclonic vorticity (Fig-

ure 9c). Again Brown chl-a mimics the responses of the Total chl-a (temperature explains most of the variance, 27.30 %).
Green chl-a shows a positive linear relationship with salinity (Figure 9i) and a dome-shape distribution with temperature (Figure 9j, 19 % of explained variance), with a maximum at slightly colder waters. The B:G ratio (Figure 9n) shows a negative correlation with salinity (11.80 % of explained variance), while temperature has a lower impact (4.50 % of explained variance).

While the GAMs at the DCM subset perform substantially worse for the Total chl-a (only 17.3 % of explained variance), they show much better performances for Brown and Green chl-a distributions, with 37.7 % and 56.9 % of explained variance, respectively. The model for the B:G ratio explains even a higher percentage of the variance, 64.5 %. Total chl-a distribution are correlated with salinity and vorticity (Figure 10a and c) and show a dome-shape relationship with temperature (Figure 10b) similar to that of APY and BPY subsets. However, the relative importance of the variables is different, vorticity explains the 9.97 % of the variance and is depicted as the main modulating environmental factor, although very close to the 8.98 % explained by salinity. These differences are reinforced for the Brown chl-a model, where salinity and temperature explain a very low percentage of the variance (with almost flat distributions, Figure 10e-f) and vorticity and vertical velocity are responsible of the 19.30 % and 4.40 % of the variance, respectively (Table 2). For the Green chl-a, the main modulating factors are salinity and vertical velocity (Figure 10i and m, 25.40 % and 10.5 % of explained variance, respectively), while the effect of vorticity is very low (Figure 10k, 4.10 %). In the case of DCM Green chl-a distribution, positive values of vertical velocity (upwelling) impact negatively the chl-a concentration. Finally, for the B:G ratio, salinity stands out as the main modulating factor, explaining 20 % of the variance. However, the effect of vertical velocities and vorticity is also considerable, with 14 % and 9.30 % of explained variance.

4 Discussion

During and around the dates of the Etoile oceanographic cruise, two cyclones (C17W and C17E) were observed in the study area by means of different multiplatform sensors. While the signature of the cyclones in the HF radar fields was not continuous (and dependent on the prevailing wind conditions), their subsurface structure could be diagnosed from the hydrographic measurements obtained during the cruise. The geostrophic circulation indicated the presence of a dipole structure formed by C17W and C17E, a frontal region of anticyclonic circulation in between, and an additional anticyclone (A17). Further, two salinity fronts, one at the near-surface (<14 m) and one at the subsurface (>50 m) were observed. From the chl-a profiles, the DCM could be located below the pycnocline at ~60 m, while the chl-a distribution of the two dominant spectral groups of algae, Brown and Green algae, was depicted. The relative importance of the environmental factors modulating the chl-a distribution was assessed by the use of GAMs. The GAMs showed not only that these environmental factors affect the Brown and Green algae differently, but also that their relative importance changes throughout the water column. While salinity and temperature explain most of the variance above and below the pycnocline of both Brown and Green chl-a, vorticity captures most of the

variance in the DCM for Brown algae.

4.1 Physical Environment

The hydrographic and hydrodynamic regimes observed at the SE-BoB during the Etoile cruise, despite being spatio-temporally highly complex, were not exceptional and similar conditions have been already recorded. The surface salinity front we encountered onshore was observed on early May 2009 by Reverdin et al. (2013). They described a fresher (34-35) and deeper ($\sim$30 m) freshwater layer originated due to winter and spring river runoff and which signal weakens towards August by increasing salinity to $\sim$35, as a result of vertical mixing and offshore advection by Ekman transport. This shelf break front is a recurrent feature in the study area, and is originated by the differences between the waters over the French shelf and the Landes Plateau and those located over the Spanish shelf and slope (Valencia et al., 2004).

Furthermore, the dipole-type structures have also been observed before in the BoB, yet in a larger scale (Pingree and Garcia-Soto, 2014; Solabarrieta et al., 2014; Caballero et al., 2016; Rubio et al., 2018). Both the location of the vertical velocities at the periphery of the structures and the magnitude (1-10 m day^{-1}) are consistent with already reported results (Mahadevan et al., 2008; Lévy et al., 2012; Caballero et al., 2016). While the cyclones were detected by the HF radar before the cruise, these were vanished during the survey due to the change in the wind-induced current regime. Their intermittent signature in the HF radar surface fields is explained by the interaction of the geostrophic and wind-induced flow. A similar situation was described using an analytical model in the Florida current by Liu et al. (2015), where a surface meandering flow was observed as a result of the overlap between a coastal jet and an eddy dipole field. This is coherent with our observations, i.e. under predominant NE winds the wind-driven circulation over the eddy field results in a meandering structure. Indeed, as the wind weakens the cyclones signature is again observed in the HF radar fields, highlighting the importance of using a wide range of multiplatform spatio-temporal data for a better characterization of the coastal hydrodynamics.

4.2 Environmental Drivers

In the BoB, coastal chl-a is highly dependent on the seasonality of riverine nutrient inputs (Guillaud et al., 2008; Borja et al., 2016; Muñiz et al., 2019). From satellite imagery and continuously recorded surface salinity and chl-a^{sat} data (Figure 3 and 6), it is evident that the Adour and Bidasoa plumes are associated with the highest chl-a concentrations in the sea surface. Simultaneously, the location of the Adour and Bidasoa plumes depends on the wind conditions, which controls the non-geostrophic surface circulation as shown by the HF radar LRC. Our results agree with the observed general pattern in which westerly winds push the river plume towards the coast, while easterly winds promote an offshore expansion (Petus et al., 2014). Thereby, the surface-most chl-a pattern is eventually dependant on the winds that modulate the position of the river plume. At subsurface, the occurrence of the DCM agrees with previously described phytoplankton distributions. Muñiz et al. (2019) described a DCM below 30 m in summer at the same sector on the BoB. Caballero et al. (2016) also reported a summer DCM at around 40 m

(below the thermocline) at the periphery of two cyclones.

355

Between the surface-most layer and the pycnocline, non-geostrophic processes related to wind-driven currents (e.g. offshore advection of coastal waters during upwelling-favourable winds) have an important role in the chl-a distribution changes, showing decreasing intensity with depth. On the contrary, below pycnocline, we could expect geostrophic currents progressively become the main driver for particle advection. These two layers are also different regarding the nutrient supply. Typically, waters above the mixed layer are depleted in nutrients, whereas below, the phytoplankton would benefit from the nutrient supply by ocean deep waters in combination with maximum light penetration in summer (Cullen, 2015). This can also lead to different phytoplankton communities with different nutrient requirements.

At APY, most of the variance of Total and Brown chl-a is explained by salinity, while the environmental variable that explains most of the Green chl-a variance is temperature. These results suggest that the Green algae is likely associated to the presence of nutrients on river plumes (fresher and warmer waters) from Adour and Bidasoa. However, the Brown algae seemed to be unaffected by the river plume, at least directly, since they display high chl-a concentration at deeper, colder and slightly saltier waters. The causative link between the environmental variables and the Brown chl-a distribution is harder to draw. Yet, salinity is the main modulating factor and might suggest an indirect link with nutrient provisioning by river runoff. At BPY, temperature is the variable that explains most of the variance. However, this could be the result of the positioning of the DCM at a specific depth and the large vertical gradient of temperature in the water column, where there would be a good compromise between light and nutrient availability (not measured during this study) for phytoplankton growth (Cullen, 2015). In fact, for the B:G ratio, this effect cancels out and salinity is the most important environmental factor. Overall, when integrating the entire water column, even though the responses differ in the different subsets, salinity is the most important environmental factor regarding the Total chl-a distribution and the relative occurrence of Brown and Green algae. We attribute this effect to salinity and its relation to nutrient content at the surface fresher and at the deeper saltier waters (Muñiz et al., 2019).

At the DCM, vorticity is the factor that explains most of the variance in Total chl-a and Brown chl-a concentrations. The more negative (positive) the vorticity, the more anticyclonic (cyclonic) is the circulation and the more positive (negative) is the effect on Brown chl-a concentrations. In anticyclones, due to Ekman transport, a small part of the flow targets the core leading to an accumulation of phytoplankton at their center (Mahadevan et al., 2008). On the contrary, Ekman transport results in an outward transport in cyclones. Therefore, C17W and C17E would have advected the Brown algae and expelled them from the core. These were then subsequently trapped in the anticyclonic circulation located between the cyclones. A similar pattern is described by Caballero et al. (2016), where the highest chl-a concentrations were located at the periphery of the cyclones. The effect of this advection by submesoscale processes is such, that the distribution of Brown algae at the DCM cannot be statistically explained without the addition of vorticity to the GAM.

However, the distribution of Green chl-a is not affected by vorticity, and the environmental factor that exerts most of the difference between the two spectral groups is salinity. From our observation we cannot explain the occurrence of a single spectral group in the core of the anticyclonic circulation. Latasa et al. (2017) demonstrated that, during the summer stratification in the Iberian Shelf and Margin, the DCM are composed of different types of phytoplankton, each of them adapted to the different existing micro-environments. However, the phytoplankton landscape organized in submesoscale patches are often dominated by a single species (D'Ovidio et al., 2010). This structuring of the phytoplankton community is a direct effect of the horizontal stirring, which can create intense patchiness in species distribution (Lévy et al., 2012). We believe that the observed submesoscale processes during the Etoile cruise would have perturbed an already existing horizontal layer of DCM, not enhancing primary production (not measured during our study) by themselves, but rather isolating, advecting and gathering the phytoplankton in the region of anticyclonic circulation.

4.3 Limitations of the study

It is worth remarking the main limitations encountered during this study, especially focusing on the Etoile cruise. The sampling area was insufficient for completely cover some of the observed structures. Similarly, having just a synoptic image of the processes and lacking temporal information (despite operational and remote sensing data) makes challenging to derive a cause-consequence relation, especially regarding the evolution of the system. Although we used chl-a as a proxy for phytoplankton biomass concentration, we note that photo-acclimation of pigment content (Cullen, 2015), which, together with variable fluorescence to chlorophyll ratios (Estrada et al., 1996; Kruskopf and Flynn, 2006; Houliez et al., 2012), could lead to elevated chl-a concentration relative to phytoplankton biomass at depth.

In addition, no further phytoplankton classification was carried out which might have helped defining specific environmental niches (D'Ovidio et al., 2010; Latasa et al., 2017) and correlating spectral groups to pigmentary groups and/or taxa. The latter is an essential issue to be considered, since the Fluoroprobe factory fingerprints are determined on mono-specific cultures or target micro-algae that are not necessarily representative to our shelf and ocean system (Houliez et al., 2012). No nutrient or light measurements were taken either; therefore, we cannot explicitly describe any inter-species competition which would have helped us understanding the ecological consequences of these submesoscale processes. A distinct spectral community structure was anyway detected, compared to the surrounding waters, which could potentially be extended through the trophic web and even affect top predator's foraging behaviour (Cotté et al., 2015; Tew Kai et al., 2009). Thus, our results suggest, that the combined effects of submesoscale features, even though concerning a relatively small fraction of the total area, may be disproportionately important to biological dynamics.

5   Conclusions

We analysed multi-platform in-situ and remote sensing data to characterize coastal submesoscale processes and their influence on the distribution of the two major phytoplankton pigmentary groups in the SE-BoB. Satellite imagery and HF radar data provided information about the surface-most layer, which was highly conditioned by the run-off of Adour and Bidasoa rivers. The location of the plume was influenced by the surface currents, which are ultimately conditioned by the speed and direction of the wind.

Multi-spectral chl-a fluorescence measurements allowed us to identify the contrasting effects of a set of environmental variables on the distribution and concentration of different phytoplankton spectral groups. From top to bottom, salinity explained most of the distribution of the chl-a for both Brown and Green algae. While salinity would still be the most important environmental driver for Green algae at the DCM, vorticity explained most of the variance of the distribution of Total chl-a and Brown chl-a at this layer. Anticyclonic circulation gathered the Brown algae in the center via Ekman transport. The effect was such that the distribution of Brown algae within the DCM could not be statistically explained without the vorticity as an environmental variable. This research brings into consideration the relevance of the dynamic variables in the study of phytoplankton, as well as the measurements of multi-spectral chl-a fluorescence at high spatial resolution. Further research providing a more detailed composition of the phytoplankton community in terms of pigments, size classes and taxonomy, together with an exhaustive analysis of the hydrodynamics, will help to better identify the ecological and functional traits of phytoplankton groups and determine their submesoscale distribution in coastal systems.

1   Appendix A: Supplementary Material

1.1   Observation of eddies after ETOILE

After the change in wind regime on August 7th the eddy C17W is again visible in the HF radar. Its has moved southwards with respect its location on July 29th. Meanwhile, C17E has vanished although it might be just masked by the surface currents since a meandering is still visible in its former location at 1.7^{o}W.

1.2   Phytoplakton Observations at T3

A cross section at the 43.70 ^{o}N out of the core of the anticyclonic frontal area, revels that this pattern is not ubiquous. Here there is not a clear dichotomy among the groups nor a deeper maximum of Green algae. Rather, there is a uniform layer of Brown algae.

Author contributions.   XD, AR, FA, IP, IMN, PL and AC contributed to the main structure and contents. In addition, XD produced the figures, AR, FA, IMN, IP and PL participated in the measurements and IP and PL coordinated the cruise.

Competing interests. The authors declare that they have no conflict of interest.

450 *Acknowledgements.* This study has been supported by the JERICO-NEXT and JERICO-S3 projects, funded by the European Union's Horizon 2020 Research and Innovation Program under grant agreement no. 654410 and 871153. SST and Chl-a data are produced and distributed by NERC Earth Observation Data Acquisition and Analysis Service (NEODAAS, https://www.neodaas.ac.uk/Access_Data). We thank the Emergencies and Meteorology Directorate – Security department – Basque Government and Euskalmet, for public provision of data from the Basque Operational Oceanography System EuskOOS. Ivan Manso-Narvarte was supported by a PhD fellowship from the Department of

455 Environment, Regional Planning, Agriculture and Fisheries of the Basque Government. We would like to thank everyone who participated in the ETOILE Campaign and has collected or processed the data as well as the "cote de la Manche" crew and Nerea Lezama for her support with the GAMs.

This is contribution number 1036 of AZTI, Marine Research, Basque Research and Technology Alliance (BRTA).

References

Benson, D. J.: Computational methods in Lagrangian and Eulerian hydrocodes, Computer Methods in Applied Mechanics and Engineering, 99, 235–394, https://doi.org/10.1016/0045-7825(92)90042-I, 1992.

Beutler, M, H, W. K., Meyer, B., Moldaenke, C., Lüring, C., Meyerhöfer, M., Hansen, U. P., and Dau, H.: A fluorometric method for the differentiation of algal populations in vivo and in situ, Photosynthesis Research, pp. 136–151, 2002.

Borja, A., Chust, G., Rodríguez, J. G., Bald, J., Belzunce-Segarra, M. J., Franco, J., Garmendia, J. M., Larreta, J., Menchaca, I., Muxika, I., Solaun, O., Revilla, M., Uriarte, A., Valencia, V., and Zorita, I.: 'The past is the future of the present': Learning from long-time series of marine monitoring, Science of The Total Environment, 566-567, 698–711, 2016.

Caballero, A., Rubio, A., Ruiz, S., Le, B., Testor, P., Mader, J., and Hernández, C.: South-Eastern Bay of Biscay eddy-induced anomalies and their effect on chlorophyll distribution, Journal of Marine Systems, pp. 1–16, https://doi.org/10.1016/j.jmarsys.2016.04.001, 2016.

Caballero, A., Mulet, S., Ayoub, N., Manso-Narvarte, I., Davila, X., Boone, C., Toublanc, F., and Rubio, A.: Integration of HF Radar Observations for an Enhanced Coastal Mean Dynamic Topography, Frontiers in Marine Science, 7, 1005, https://doi.org/10.3389/fmars.2020.588713, 2020.

Cotté, C., D'Ovidio, F., Dragon, A. C., Guinet, C., and Lévy, M.: Flexible preference of southern elephant seals for distinct mesoscale features within the Antarctic Circumpolar Current, Progress in Oceanography, 131, 46–58, https://doi.org/10.1016/j.pocean.2014.11.011, 2015.

Cullen, J. J.: Subsurface Chlorophyll Maximum Layers: Enduring Enigma or Mystery Solved?, Annual Review of Marine Science, 7, 207–239, https://doi.org/10.1146/annurev-marine-010213-135111, 2015.

D'Ovidio, F., De Monte, S., Alvain, S., Dandonneau, Y., and Levy, M.: Fluid dynamical niches of phytoplankton types, Proceedings of the National Academy of Sciences, 107, 18 366–18 370, https://doi.org/10.1073/pnas.1004620107, 2010.

Emery, W. J. and Thomson, R. E.: Preface, in: Data Analysis Methods in Physical Oceanography, edited by Emery, W. J. and Thomson, R. E., Elsevier Science, Amsterdam, https://doi.org/https://doi.org/10.1016/B978-044450756-3/50000-9, 2001.

Estrada, M., Marrasé, C., and Salat, J.: In vivo fluorescence/chlorophyll a ratio as an ecological indicator in oceanography, Sci. Mar., pp. 317–325, 1996.

Fernández, E., Cabal, J., Acuña, J. L., Bode, A., Botas, A., and García-soto, C.: Plankton distribution across a slope current-induced front in the southern Bay of Biscay, Journal of Plankton Research, 15, 619–641, https://doi.org/10.1093/plankt/15.6.619, 1993.

Ferrer, L., Fontán, A., Mader, J., Chust, G., González, M., Valencia, V., Uriarte, A., and Collins, M. B.: Low-salinity plumes in the oceanic region of the Basque Country, Continental Shelf Research, 29, 970–984, https://doi.org/10.1016/j.csr.2008.12.014, 2009.

Gomis, D. and Ruiz, S.: Manual DAToBJETIVO v.01: Una herramienta para el análisis espacial objetivo y diagnóstico de variables oceanográficas. Departamento Recursos Naturales, Grupo de Oceanografía Interdisciplinar IMEDEA (centro mixto Universitat de les Illes Balears - CSIC), Mallorca, España., 2003.

Gomis, D., Ruiz, S., and Pedder, M. A.: Diagnostic analysis of the 3D ageostrophic circulation from a multivariate spatial interpolation of CTD and ADCP data, Deep-Sea Research Part I: Oceanographic Research Papers, 48, 269–295, https://doi.org/10.1016/S0967-0637(00)00060-1, 2001.

Gruber, N., Lachkar, Z., Frenzel, H., Marchesiello, P., Münnich, M., McWilliams, J. C., Nagai, T., and Plattner, G. K.: Eddy-induced reduction of biological production in eastern boundary upwelling systems, Nature Geoscience, 4, 787–792, https://doi.org/10.1038/ngeo1273, 2011.

Guillaud, J.-f., Aminot, A., Delmas, D., Gohin, F., Lunven, M., Labry, C., and Herbland, A.: Seasonal variation of riverine nutrient inputs in the northern Bay of Biscay (France), and patterns of marine phytoplankton response, 72, 309–319, https://doi.org/10.1016/j.jmarsys.2007.03.010, 2008.

Hastie, T. and Tibshirani, R.: Generalized Additive Models, Chapman and Hall, 1990.

500 Houliez, E., Lizon, F., Thyssen, M., Artigas, L. F., and Schmitt, F.: CSpectral fluorometric characterization of Haptophyte dynamics using the FluoroProbe: an application in the eastern English Channel for monitoring Phaeocystis globosa, J. Plankton Research, pp. 136–151, 2012.

Irigoien, X., Fiksen, Cotano, U., Uriarte, A., Alvarez, P., Arrizabalaga, H., Boyra, G., Santos, M., Sagarminaga, Y., Otheguy, P., Etxebeste, E., Zarauz, L., Artetxe, I., and Motos, L.: Could Biscay Bay Anchovy recruit through a spatial loophole?, Progress in Oceanography, 74,

505 132–148, https://doi.org/10.1016/j.pocean.2007.04.011, 2007.

Kruskopf, M. and Flynn, K. J.: Chlorophyll content and fluorescence responses cannot be used to gauge reliably phytoplankton biomass, nutrient status or growth rate, New Phytologist, pp. 525–536, 2006.

Latasa, M., Cabello, A. M., Morán, X. A. G., Massana, R., and R, S.: Distribution of phytoplankton groups within the deep chlorophyll maximum, Limnology and Oceanography, pp. 665–685, https://doi.org/10.1002/lno.10452, 2017.

510 Lévy, M., Ferrari, R., Franks, P. J., Martin, A. P., and Rivière, P.: Bringing physics to life at the submesoscale, Geophysical Research Letters, 39, 1–13, https://doi.org/10.1029/2012GL052756, 2012.

Liu, Y., Kerkering, H., and Weisberg, R.: Chapter 11 - Observing Frontal Instabilities of the Florida Current Using High Frequency Radar, in: Coastal Ocean Observing Systems, edited by Liu, Y., Kerkering, H., and Weisberg, R. H., pp. 179–208, Academic Press, Boston, https://doi.org/10.1016/B978-0-12-802022-7.00011-0, 2015.

515 Llope, M., Chan, K., and Reid, P. C.: Effects of environmental conditions on the seasonal distribution of phytoplankton biomass in the North Sea, 54, 512–524, 2009.

MacIntyre, H. L., Lawrenz, E., and Richardson, T. L.: Taxonomic Discrimination of Phytoplankton by Spectral Fluorescence, in: Chlorophyll a Fluorescence in Aquatic Sciences: Methods and Applications, edited by Suggett, D., Prášil, O., and Borowitzka, M., vol. 4, pp. 129–169, Developments in Applied Phycology, 2010.

520 Mahadevan, A.: Ocean science: Eddy effects on biogeochemistry, Nature, 506, 168–169, https://doi.org/10.1038/nature13048, 2014.

Mahadevan, A.: The Impact of Submesoscale Physics on Primary Productivity of Plankton, Annual Review of Marine Science, 8, https://doi.org/10.1146/annurev-marine-010814-015912, 2016.

Mahadevan, A., Thomas, L. N., and Tandon, A.: Comment on "eddy/wind interactions stimulate extraordinary mid-ocean plankton blooms", Science, 320, https://doi.org/10.1126/science.1148974, 2008.

525 Mantovani, C., Corgnati, L., Horstmann, J., Rubio, A., Reyes, E., Quentin, C., Cosoli, S., Asensio, J. L., Mader, J., and Griffa, A.: Best Practices on High Frequency Radar Deployment and Operation for Ocean Current Measurement, Frontiers in Marine Science, 7, 2020.

Morozov, E., Pozdnyakov, D., Smyth, T., Sychev, V., and Grassl, H.: Space-borne study of seasonal, multi-year, and decadal phytoplankton dynamics in the Bay of Biscay, International Journal of Remote Sensing, 34, 1297–1331, https://doi.org/10.1080/01431161.2012.718462, 2013.

530 Muller, H., Blanke, B., Dumas, F., Lekien, F., and Mariette, V.: Estimating Lagrangian Residual Circulation (LRC) in the Iroise Sea, Proceedings of the IEEE Working Conference on Current Measurement Technology, 78, 279–284, https://doi.org/10.1109/CCM.2008.4480881, 2009.

Muñiz, O., Revilla, M., Rodríguez, J. G., Laza-Martínez, A., and Fontán, A.: Annual cycle of phytoplankton community through the water column: Study applied to the implementation of bivalve offshore aquaculture in the southeastern Bay of Biscay, Oceanologia, 61, 114–130, 2019.

Petus, C., Marieu, V., Novoa, S., Chust, G., Bruneau, N., and Froidefond, J. M.: Monitoring spatio-temporal variability of the Adour River turbid plume (Bay of Biscay, France) with MODIS 250-m imagery, Continental Shelf Research, 74, 35–49, https://doi.org/10.1016/j.csr.2013.11.011, 2014.

Pingree, R. D. and Garcia-Soto, C.: Plankton blooms, ocean circulation and the European slope current: Response to weather and climate in the Bay of Biscay and W English Channel (NE Atlantic), Deep-Sea Research Part II: Topical Studies in Oceanography, 106, 5–22, https://doi.org/10.1016/j.dsr2.2014.07.008, 2014.

Puillat, I., Lazure, P., Jégou, A.-m., Lampert, L., and Miller, P.: Mesoscale hydrological variability induced by northwesterly wind on the French continental shelf of the Bay of Biscay, pp. 15–26, 2006.

R Core Team: R: A Language and Environment for Statistical Computing, R Foundation for Statistical Computing, Vienna, Austria, https://www.R-project.org/, 2020.

Reverdin, G., Marié, L., Lazure, P., Ovidio, F., Boutin, J., Testor, P., Martin, N., Lourenco, A., Gaillard, F., Lavin, A., Rodriguez, C., Somavilla, R., Mader, J., Rubio, A., Blouch, P., Rolland, J., Bozec, Y., Charria, G., Batifoulier, F., Dumas, F., Louazel, S., and Chanut, J.: Freshwater from the Bay of Biscay shelves in 2009, Journal of Marine Systems, 109-110, S134–S143, https://doi.org/10.1016/j.jmarsys.2011.09.017, 2013.

Rubio, A., Reverdin, G., Fontán, A., González, M., and Mader, J.: Mapping near-inertial variability in the SE Bay of Biscay from HF radar data and two offshore moored buoys, GRL, 38, 2011.

Rubio, A., Solabarrieta, L., Castanedo, S., Medina, R., and Aranda, J. A.: SE Bay of Biscay from HF radar data, 2013.

Rubio, A., Caballero, A., Or, A., Hernández-carrasco, I., Ferrer, L., González, M., Solabarrieta, L., and Mader, J.: Remote Sensing of Environment Eddy-induced cross-shelf export of high Chl-a coastal waters in the SE Bay of Biscay, 205, 290–304, https://doi.org/10.1016/j.rse.2017.10.037, 2018.

Solabarrieta, L., Rubio, A., Castanedo, S., Medina, R., Charria, G., and Hernández, C.: Surface water circulation patterns in the southeastern Bay of Biscay : New evidences from HF radar data, Continental Shelf Research, 74, 60–76, https://doi.org/10.1016/j.csr.2013.11.022, 2014.

Teles-Machado, A., Peliz, A., McWilliams, J. C., Dubert, J., and LeCann, B.: Circulation on the Northwestern Iberian Margin: Swoddies, Progress in Oceanography, 140, 116–133, 2016.

Tew Kai, E., Rossi, V., Sudre, J., Weimerskirch, H., Lopez, C., Hernandez-Garcia, E., Marsac, F., and Garçon, V.: Top marine predators track Lagrangian coherent structures, Proceedings of the National Academy of Sciences of the United States of America, 106, 8245–8250, https://doi.org/10.1073/pnas.0811034106, 2009.

Valencia, V., Franco, J., Borja, Á., and Fontán, A.: Hydrography of the southeastern Bay of Biscay, Oceanography and marine environment of the Basque Country, pp. 159–194, https://doi.org/10.1016/S0422-9894(04)80045-X, 2004.

Wood, S. N.: Modelling and smoothing parameter estimation with multiple quadratic penalties, J. R. Stat. Soc., 62, 413–428, 2000.

Wood, S. N.: Generalized additive models: An introduction with R, Chapman Hall/CRC, 2006.

Wood, S. N.: Fast stable restricted maximum likelihood and marginal likelihood estimation of semiparametric generalized linear models, Journal of the Royal Statistical Society, pp. 3–36, 2011.
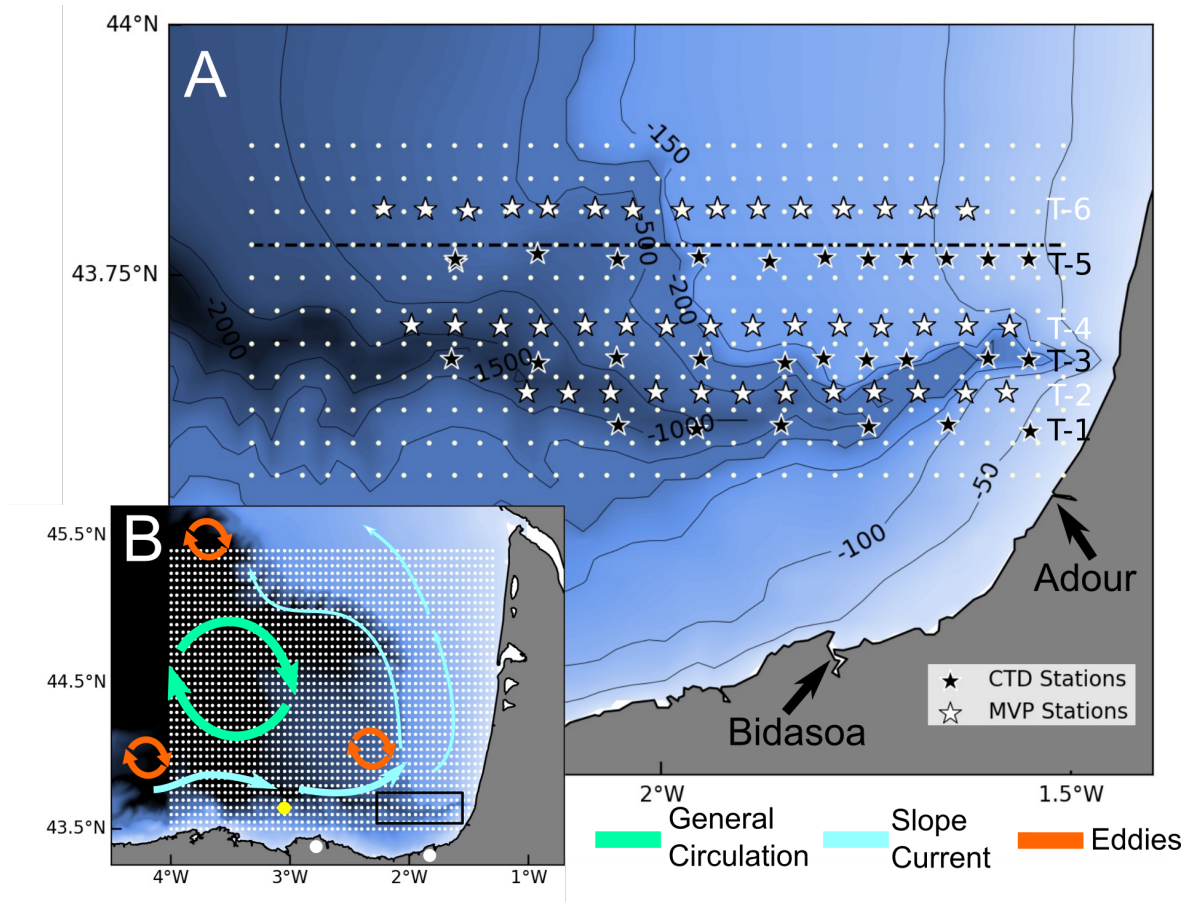
Figure 1. Sampling map and circulation in the Bay of Biscay. Location of the CTD and Moving Vessel Profiler (MVP) stations (A). At uneven transects (T-1, T-3 and T-5) black stars mark the CTD stations where vertical casts of temperature, salinity and in vivo multi-spectral chlorophyll-a (chl-a) fluorescence were collected. At even transects, white stars mark the location of the point at which MVP data has been averaged, located every 5 km. White dots represent the grid at which these measurements were interpolated and the black dashed line marks the cross-section at 43.77°N analysed in Figures 5 and 7. The location of the rivers Adour and Bidasoa is shown by the black arrows. Seasonal to mesoscale circulation in the Bay of Biscay (B). The small white dots represent the HF radar grid, the yellow dot corresponds to the location of the oceano-metereological buoy used for the wind data, and large white dots mark the location of the HF radar antennas. The black rectangle shows the area covered by the in-situ sampling during Etoile survey, which is zoomed in A.
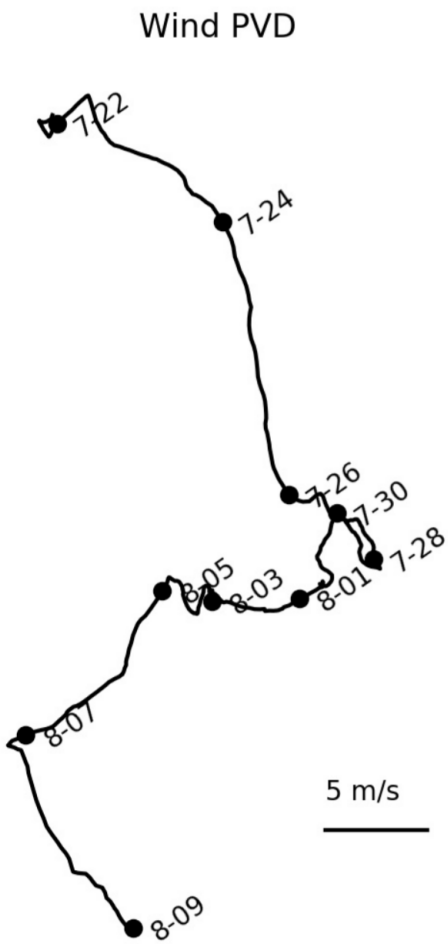
Figure 2. Wind direction and intensity at Bilbao's mooring buoy represented on a Progressive Vector Diagram (PVD)
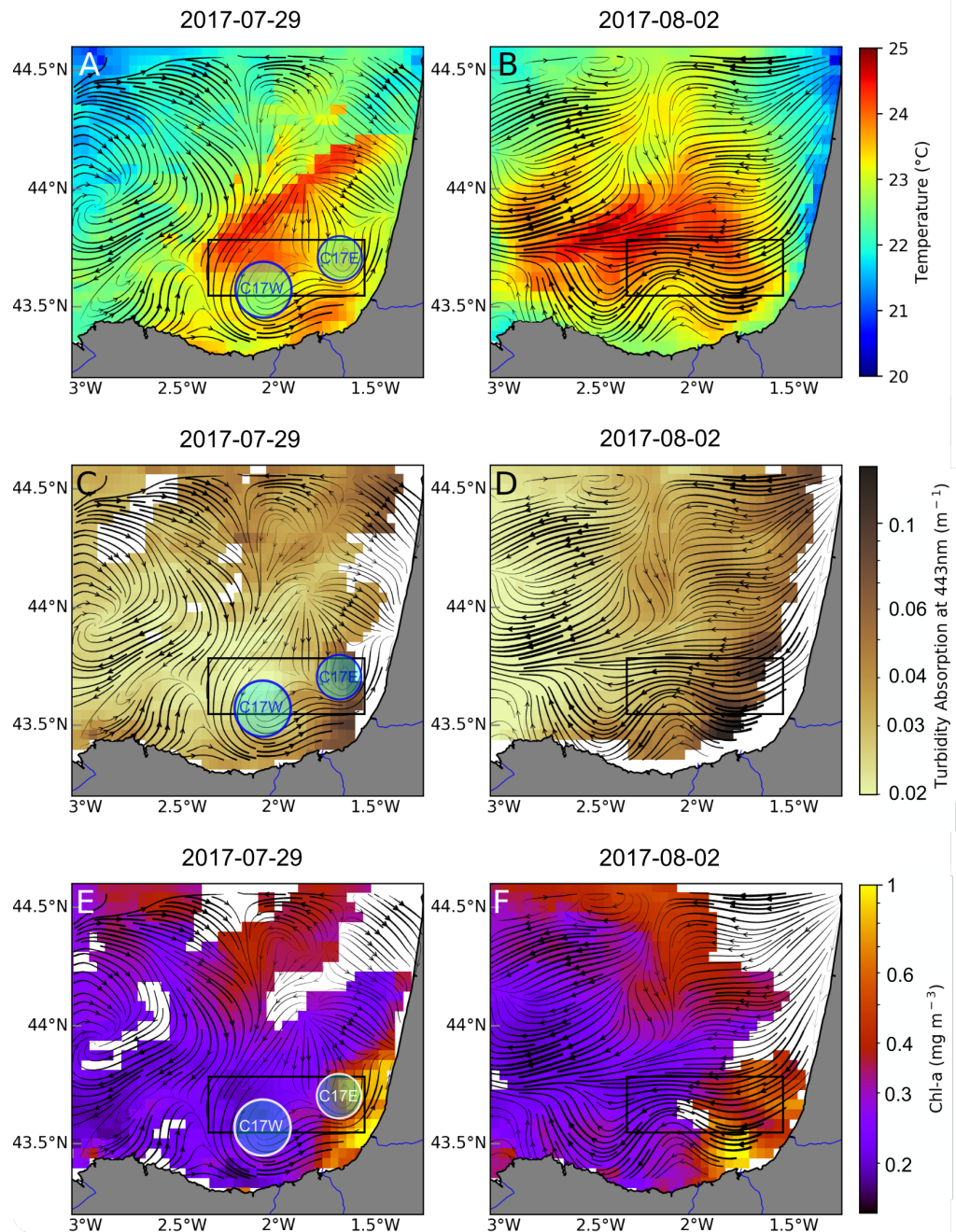
Figure 3. Satellite observations for SST (A,B), turbidity (C,D) and chl-a^{sat} (E,F) corresponding to July 29th (left column) and August 2nd (right column). Black lines show the Lagrangian Residual Currents (LRC) calculated the periods: July 26-29th and July 30th to August 2nd. The black box shows the study area, where Etoile survey took place. The circles in the left column represent the approximate location of the observed cyclonic eddies (C17W and C17E). Turbidity and chl-a are plotted on logarithmic scale.
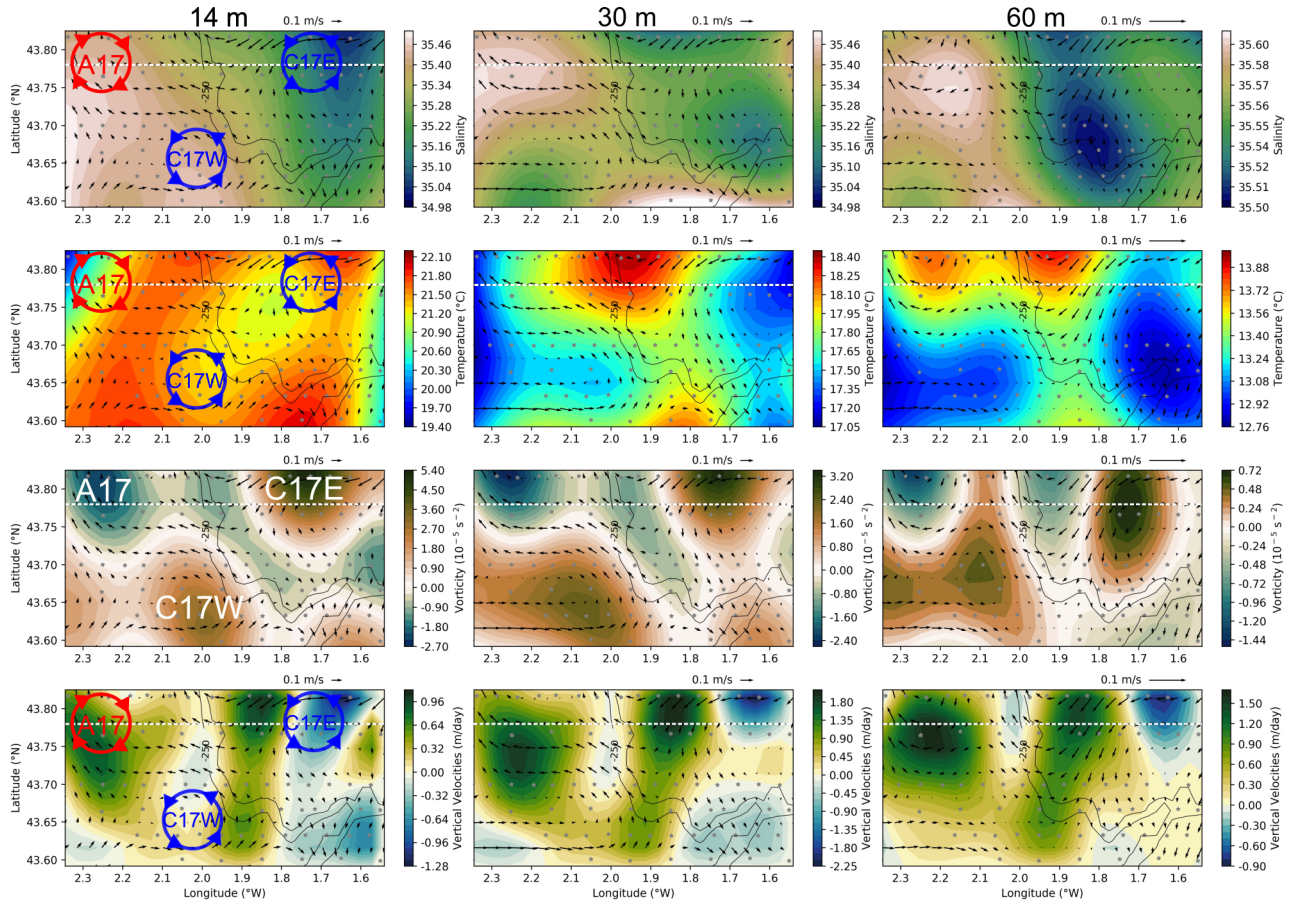
Figure 4. Synoptic plots for the hydrographic and hydrodynamical conditions for the period (August 2nd to 4th 2017). From top to bottom: salinity, temperature, vorticity and vertical velocity fields, at 14, 30 and 60 m (left to right). Black arrows correspond to the geostrophic velocities and black contours represent the 200 m and 250 m isobahts. The white dashed line corresponds to the cross section at 43.77°N shown in Figures 5 and 7. Negative vorticity values represents anticyclonic circulation while positive values represent cyclonic circulation. Negative (positive) vertical velocity values represent downwelling (upwelling). The red (blue) circles drawn in the left column represent the approximate location of A17 (C17W and C17E). The scale range for each of the variables is different for each depth.
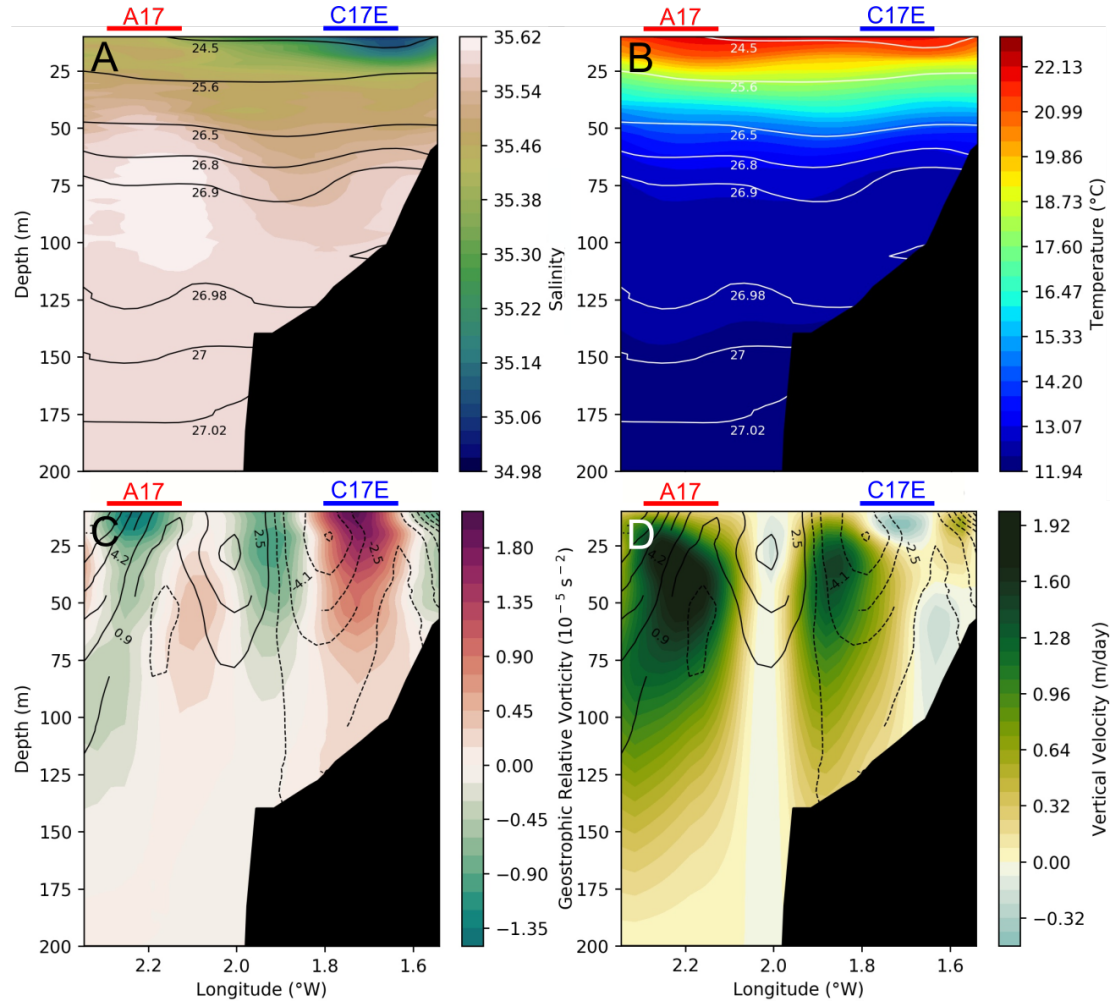
Figure 5. Cross section at 43.77°N (location marked by dashed lines in Figure 1 and 4), representing salinity (A) and temperature (B) with isopycnals (black and white contours, respectively), vorticity (C) and vertical velocities (D) with meridional geostrophic velocities (solid (dashed) black contours for positive (negative) velocities) for the period (August 2nd to 4th 2017). Negative vorticity values represents anticyclonic circulation while positive values represent cyclonic circulation. Positive (negative) values for geostrophic velocity represent northward (southward) current. Negative (positive) vertical velocity values represent downwelling (upwelling). The red (blue) horizontal lines represent the horizontal extension of A17 (C17E) that the section crosses.
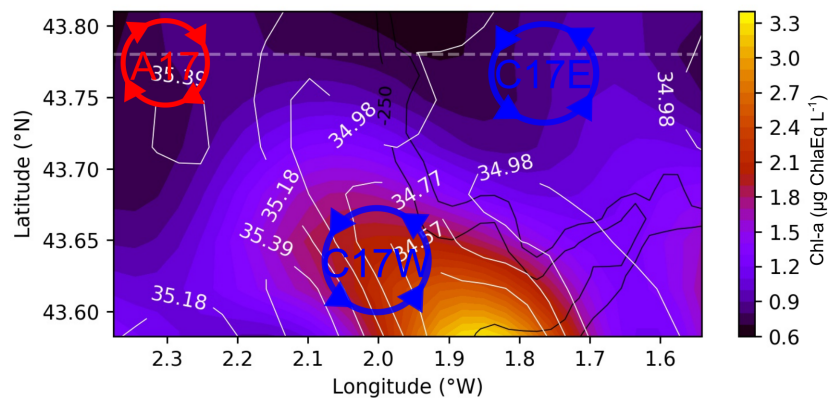
Figure 6. Surface chl-a at 3.5 m from the surface Fluoroprobe for the period (August 2nd to 4th 2017). White contours represent the salinity field while black ones the 200 m and 250 m isobaths. The red (blue) circles in the left column represent the approximate location of A17 (C17W and C17E).
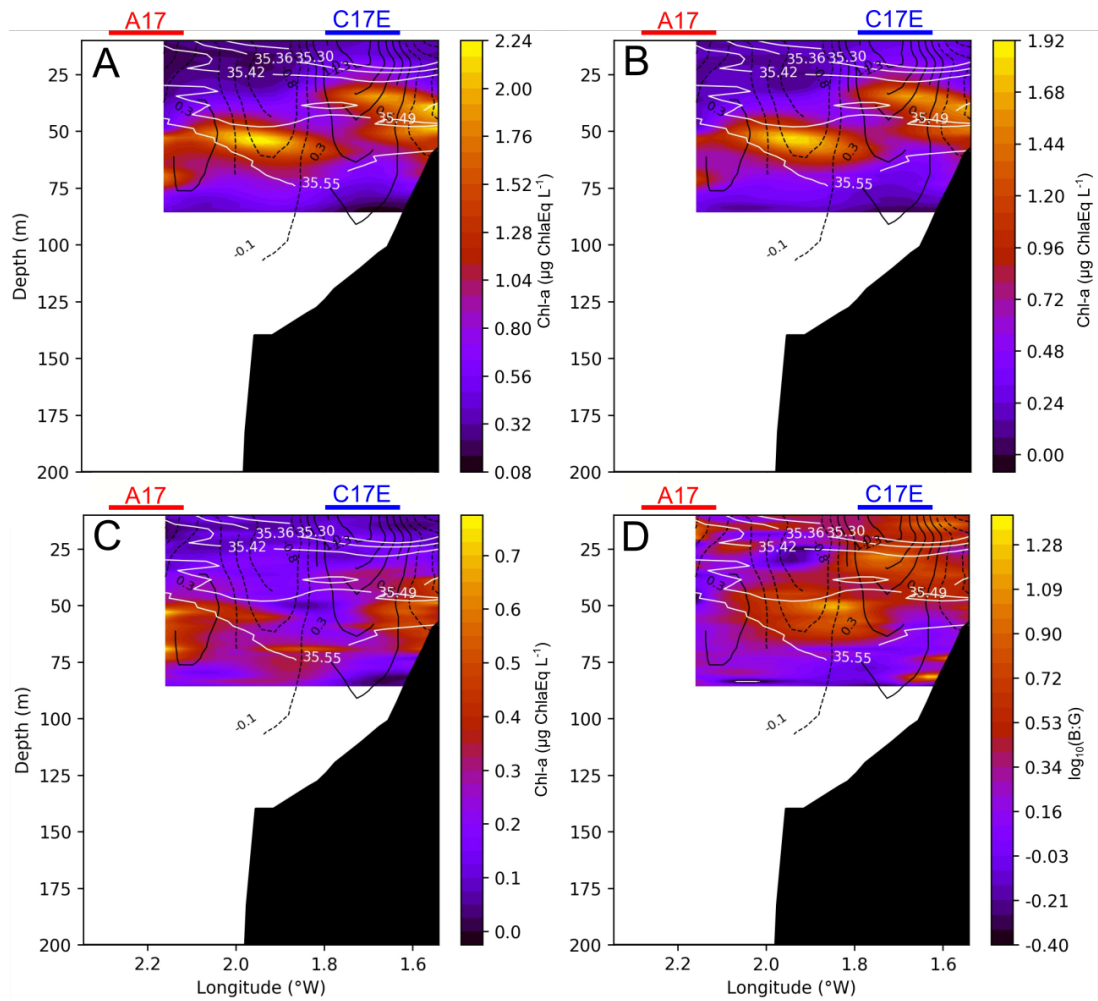
Figure 7. Cross section at 43.77°N (location marked by dashed lines in Figure 1 and 4; same section than in Figure 5) of Total chl-a (A), Brown chl-a (B), Green chl-a (C) and the Brown chl-a to Green chl-a ratio (B:G) logarithmically transformed (D) for the period (August 2nd to 4th 2017). White lines represent salinity contours and black solid lines represent positive vorticity values or cyclonic circulation, while dashed lines represent negative vorticity values of anticyclonic circulation. The red and blue horizontal lines represent the horizontal extension of A17 and C17E, respectively, that the section crosses.
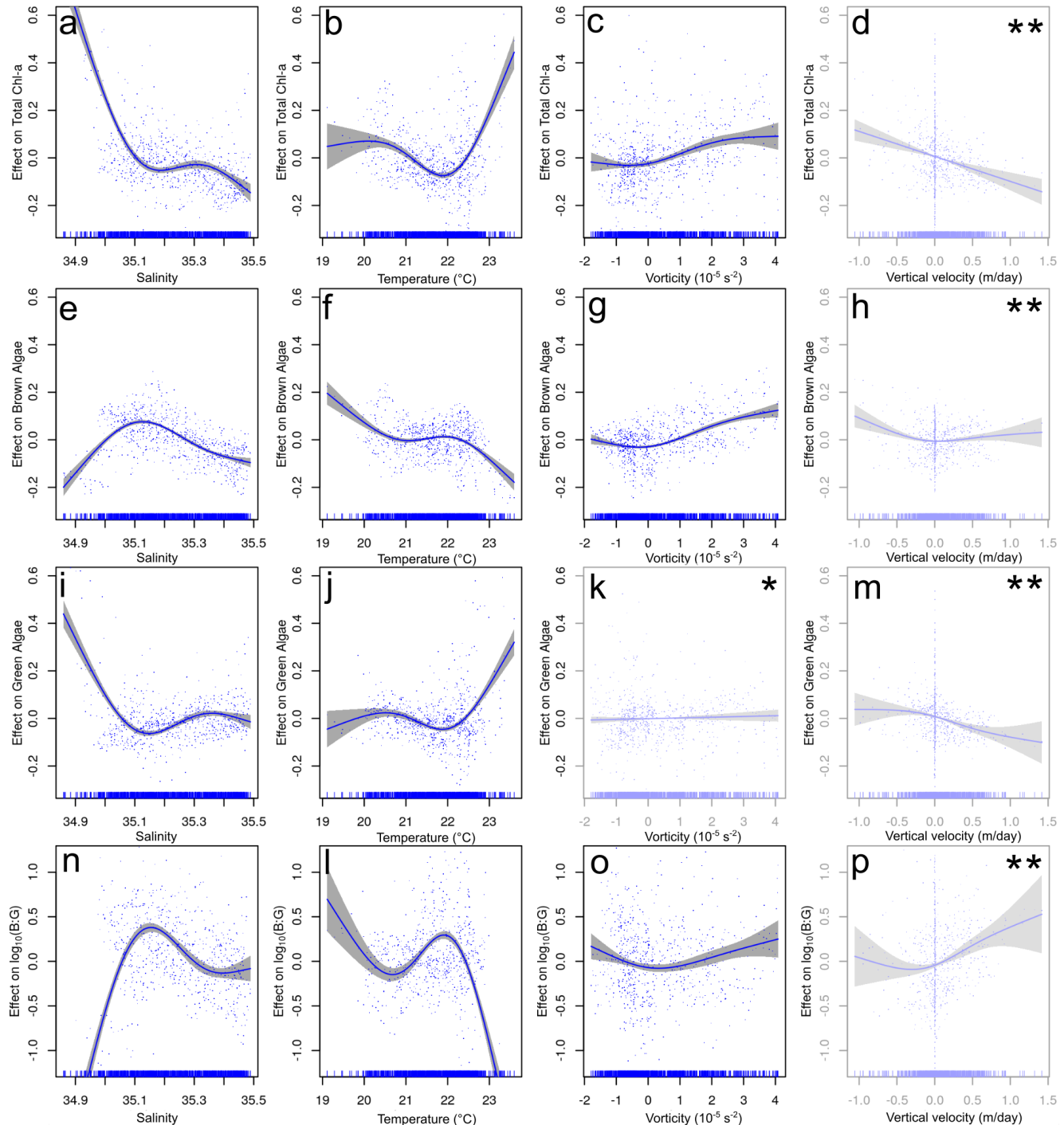
Figure 8. Relationship between environmental variables and chl-a from the Above the Pycnocline (APY) subset GAMs. The y-axis indicates the additive effect that the term on the x-axis has on the chl-a. From top to bottom, Total chl-a, Brown chl-a, Green chl-a and the Brown chl-a to Green chl-a ratio (B:G). Shaded area represents the confidence interval of 95%. The effect of vorticity for Green-algae chl-a is the only non-significant response (marked by *). The effect of vertical velocity is shown here but not analysed further since this variable is strongly influenced (in the APY subset) by the proximity to the surface layer boundary condition assumed for its calculation (marked by **).
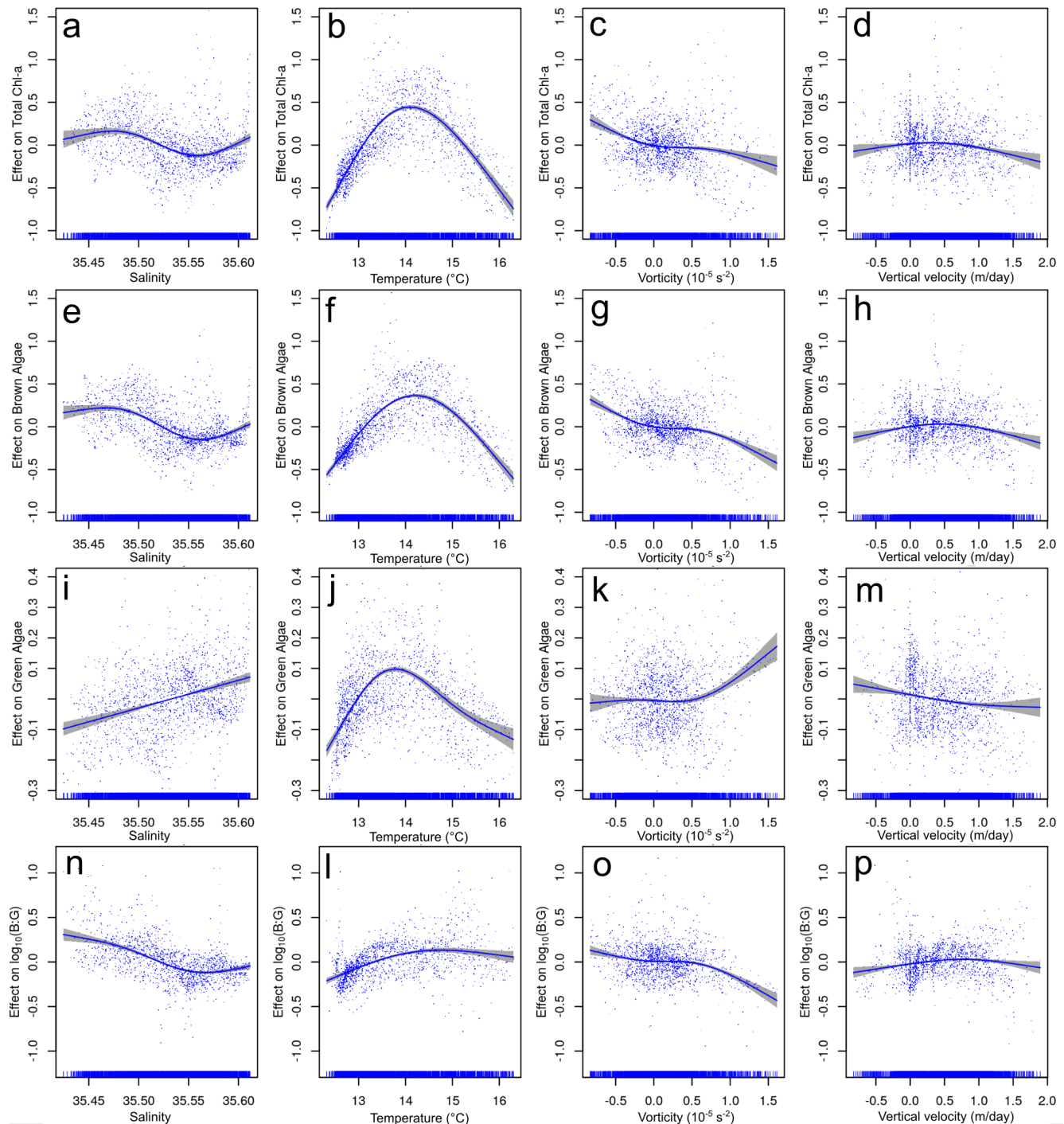
Figure 9. Relationship between environmental variables and chl-a from the Below the Pycnocline (BPY) subset GAMs. The y-axis indicates the additive effect that the term on the x-axis has on the chl-a. From top to bottom, Total chl-a, Brown chl-a, Green chl-a and the Brown:Green (B:G) ratio. Shaded area represents the confidence interval of 95%.
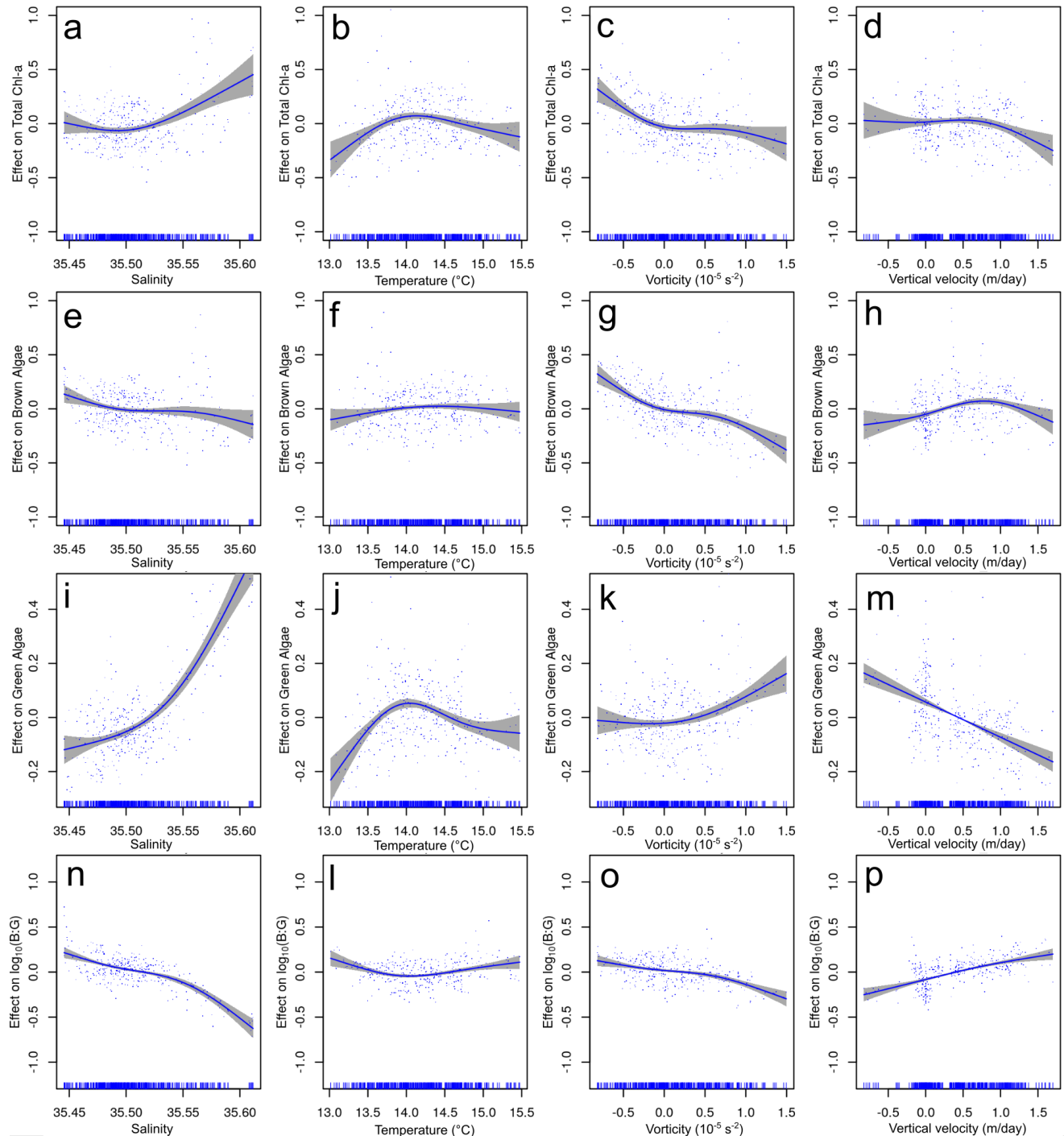
Figure 10. Relationship between environmental variables and chl-a from the Deep Chlorophyll Maximum (DCM) subset GAMs. The y-axis indicates the additive effect that the term on the x-axis has on the chl-a. From top to bottom, Total chl-a, Brown chl-a, Green chl-a and the Brown:Green (B:G) ratio. Shaded area represents the confidence interval of 95 %.
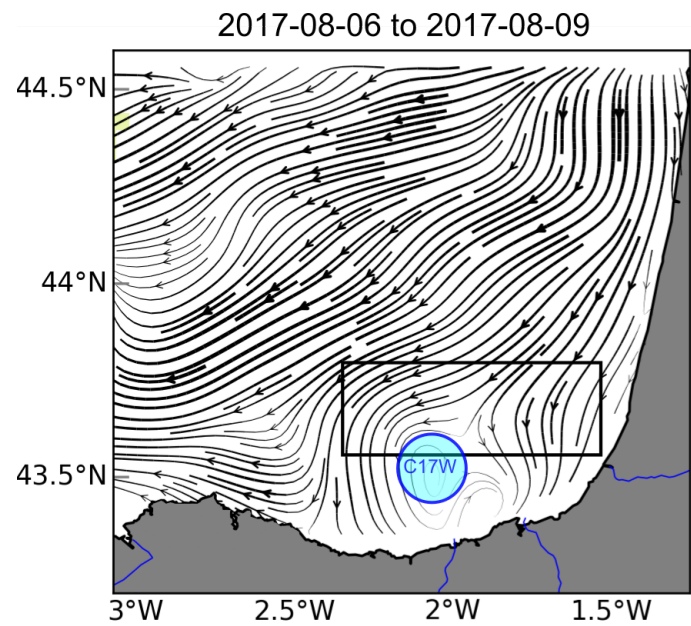
Figure A1. Lagrangian Residual Currents (LRC) for the period of August 6th to 9th, the persistent C17W eddy is still visible after the change in wind regime.
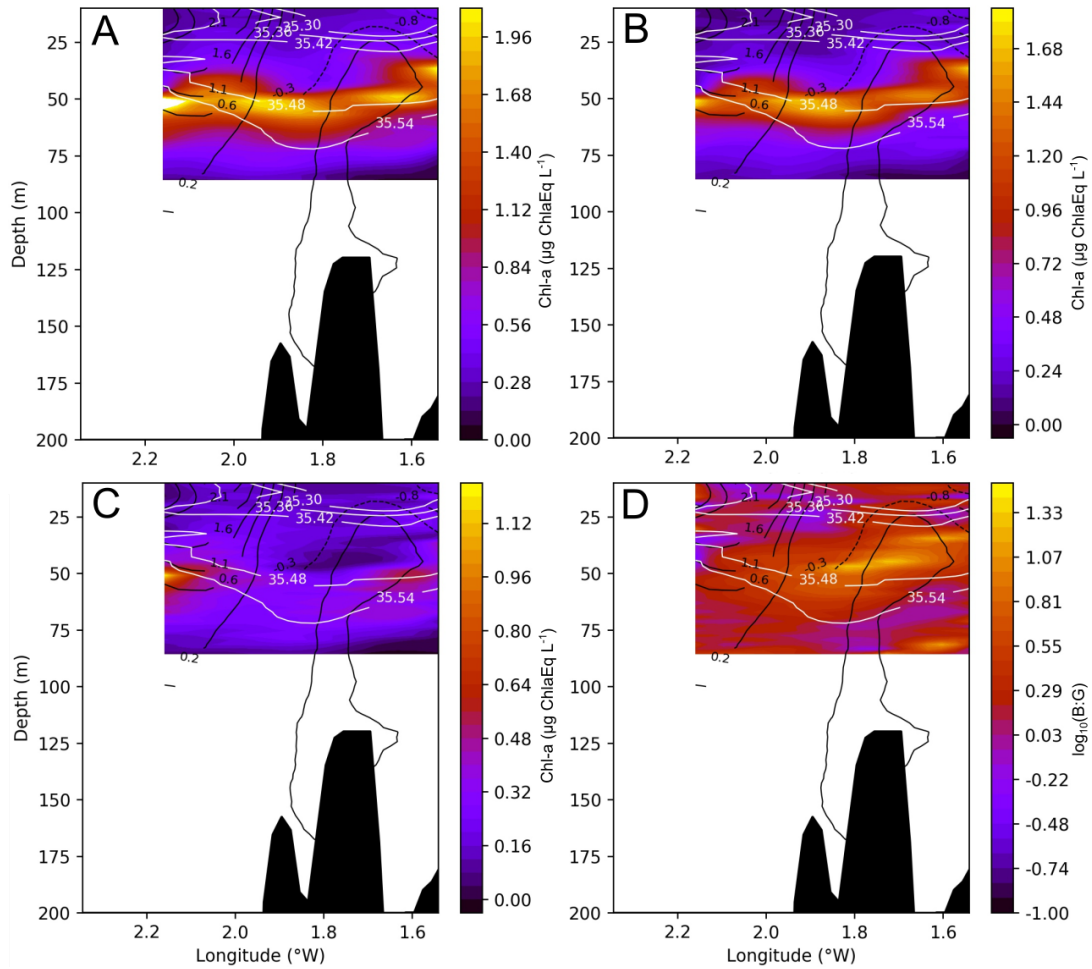
Figure A2. Cross section at 43.70^{o}N of Total chl-a(A), Brown chl-a (B), Green chl-a (C) and the Brown:Green (B:G) ratio logarithmically transformed (D). White lines represent salinity contours and black solid (dashed) lines represent positive (negative) vorticity values or cyclonic (anticyclonic) circulation.

Table 1. Generalized Additive Model (GAM) results. Intercept, standard error (SE), significance (p-value) and explained variance (%) of the GAMs for the water column sections "Above the pycnocline" (APY), "Below the pycnocline" (BPY) and at the Deep Chlorophyll Maximum (DCM). Dependant variables are the estimated chl-a concentrations for the different algae groups and B:G refers to the Brown chl-a to Green chl-a ratio. The estimated degrees of freedom (edf) and significance (p-value) of the environmental variables are also included. Although salinity and temperature were correlated for the section BPY, both variables were kept since the fit (R^2 and GCV) was better in all cases.

		APY		BPY		DCM	
		Estimate	**p-value**	**Estimate**	**p-value**	**Estimate**	**p-value**
Total Chl-a	Intercept	0.380	<0.001	1.096	<0.001	1.793	<0.001
	SE	0.0050		0.0006		0.0120	
	%	60.8		66.0		17.3	
	GCV	0.020		0.069		0.051	
		edf	**p-value**	**edf**	**p-value**	**edf**	**p-value**
	Vertical_vel	1.000	<0.001	2.461	<0.001	2.618	0.009
	Temperature	2.979	<0.001	2.972	<0.001	2.851	<0.001
	Vorticity	2.788	<0.001	2.896	<0.001	2.744	<0.001
	Salinity	2.990	<0.001	2.974	<0.001	2.484	<0.001
Brown chl-a		**Estimate**	**p-value**	**Estimate**	**p-value**	**Estimate**	**p-value**
	Intercept	0.206	<0.001	0.775	<0.001	1.374	<0.001
	SE	0.0030		0.0060		0.0091	
	%	57.1		71.8		37.7	
	GCV	0.051		0.044		0.030	
		edf	**p-value**	**edf**	**p-value**	**edf**	**p-value**
	Vertical_vel	2.658	<0.001	2.650	<0.001	2.844	<0.001
	Temperature	2.988	<0.001	2.981	<0.001	2.025	0.093
	Vorticity	2.934	<0.001	2.960	<0.001	2.816	<0.001
	Salinity	2.983	<0.001	2.970	<0.001	2.596	0.004
Green chl-a		**Estimate**	**p-value**	**Estimate**	**p-value**	**Estimate**	**p-value**
	Intercept	0.148	<0.001	0.321	<0.001	0.418	<0.001
	SE	0.0040		0.0026		0.0058	
	%	43.0		34.1		56.9	
	GCV	0.013		0.012		0.012	
		edf	**p-value**	**edf**	**p-value**	**edf**	**p-value**
	Vertical_vel	2.353	<0.001	1.924	<0.001	1.000	<0.001
	Temperature	2.983	<0.001	2.988	<0.001	2.978	<0.001
	Vorticity	1.000	0.362	2.871	<0.001	2.263	<0.001
	Salinity	2.986	<0.001	1.000	<0.001	2.784	<0.001
B:G		**Estimate**	**p-value**	**Estimate**	**p-value**	**Estimate**	**p-value**
	Intercept	0.109	<0.001	0.361	<0.001	0.543	<0.001
	SE	0.0189		0.0044		0.0063	
	%	55.0		57.2		64.5	
	GCV	0.283		0.034		0.015	
		edf	**p-value**	**edf**	**p-value**	**edf**	**p-value**
	Vertical_vel	2.452	<0.001	2.588	<0.001	1.866	<0.001
	Temperature	2.996	<0.001	2.712	<0.001	2.874	<0.001
	Vorticity	2.572	0.056	2.941	<0.001	2.652	<0.001
	Salinity	2.983	<0.001	2.935	<0.001	2.819	<0.001

Table 2. Variance contribution of the environmental variables to the estimated chl-a concentrations for the different algae groups and Brown:Green (B:G) ratio and the subsets "Above the pycnocline" (APY), "Below the pycnocline" (BPY) and at the Deep Chlorophyll Maximum (DCM). The left columns in each of the sections show these values for the models after stepwise deletion of the variables listed to the left (first vertical velocities and then temperature). The coefficient of determination (R^2) and general cross validation score (GCV) and the percentage of variance (%) correspond to the different models. The last two models included only the variable listed (vorticity or salinity). For the right columns in each section, one variable (those listed on the left) was removed at a time while keeping the rest. While R^2 and GCV still refer to the whole model, % is individual and corresponds only to the removed variable. Bold numbers point out the main modulating variable -i.e. The one that, individually, explains most of the variance in the model.

		APY Stepwise Deletion			APY Delete-one-covariance			BPY Stepwise Deletion			BPY Delete-one-covariance			DCM Stepwise Deletion			DCM Delete-one-covariance		
		R^2	GCV	%	R^2	GCV	%	R^2	GCV	%	R^2	GCV	%	R^2	GCV	%	R^2	GCV	%
Total Chl-a	All (total)	0.60	0.020					0.66	0.069					0.15	0.052				
	Vertical_vel	0.59	0.021	1.40	0.59	0.021	1.40	0.65	0.070	0.60	0.65	0.070	0.60	0.12	0.055	3.40	0.12	0.055	3.40
	Temperature	0.46	0.027	58.91	0.51	0.025	9.80	0.32	0.138	34.20	0.32	0.138	**34.00**	0.08	0.057	7.88	0.09	0.057	6.30
	Vorticity	0.02	0.077	11.50	0.58	0.022	2.50	0.06	0.184	59.62	0.64	0.073	2.10	0.05	0.058	11.07	0.06	0.059	**9.97**
	Salinity	0.46	0.027	14.40	0.47	0.042	**13.10**	0.30	0.140	35.50	0.64	0.073	2.20	0.02	0.060	15.45	0.07	0.058	8.98
Brown chl-a	All (total)	0.56	0.005					0.72	0.044					0.36	0.031				
	Vertical_vel	0.55	0.005	1.20	0.55	0.005	1.20	0.71	0.046	0.70	0.71	0.046	0.70	0.32	0.033	4.40	0.32	0.032	4.40
	Temperature	0.46	0.006	10.30	0.49	0.006	7.50	0.44	0.088	27.70	0.44	0.087	**27.30**	0.30	0.033	6.60	0.35	0.031	0.70
	Vorticity	0.29	0.008	28.00	0.44	0.007	12.40	0.09	0.143	63.11	0.68	0.051	4.00	0.26	0.035	11.10	0.17	0.039	**19.30**
	Salinity	0.14	0.010	43.30	0.33	0.008	**23.30**	0.42	0.091	29.70	0.63	0.058	8.80	0.08	0.043	28.69	0.34	0.032	1.60
Green chl-a	All (total)	0.42	0.013					0.01	0.034					0.56	0.012				
	Vertical_vel	0.40	0.013	2.00	0.40	0.013	2.00	0.33	0.012	1.3	0.33	0.012	1.3	0.46	0.015	10.50	0.46	0.015	10.5
	Temperature	0.30	0.015	12.70	0.32	0.015	**10.40**	0.13	0.015	20.5	0.14	0.015	**19.90**	0.43	0.016	13.00	0.50	0.014	6.00
	Vorticity	0.01	0.044	41.64	0.42	0.013	0.00	0.04	0.017	30.15	0.64	0.073	2.10	0.21	0.022	36.20	0.52	0.014	4.10
	Salinity	0.30	0.015	12.70	0.43	0.026	0.00	0.01	0.016	24.56	0.31	0.012	2.80	0.37	0.017	19.20	0.30	0.020	**25.40**
B:G	All (total)	0.54	0.283					0.57	0.034					0.64	0.015				
	Vertical_vel	0.53	0.289	1.30	0.53	0.289	1.30	0.56	0.035	1.00	0.56	0.035	1.00	0.50	0.020	14.00	0.50	0.020	14.00
	Temperature	0.37	0.385	17.30	0.39	0.379	**15.80**	0.51	0.038	5.80	0.53	0.038	4.50	0.50	0.020	14.20	0.60	0.016	3.40
	Vorticity	0.02	0.657	52.46	0.54	0.287	1.00	0.08	0.721	48.58	0.53	0.037	4.20	0.30	0.028	34.10	0.54	0.018	9.30
	Salinity	0.63	0.392	18.70	0.39	0.414	15.60	0.48	0.409	9.10	0.45	0.043	**11.80**	0.32	0.027	31.70	0.43	0.023	**20.00**